Supplementary Information (SI) for Journal of Materials Chemistry A.
This journal is © The Royal Society of Chemistry 2026

Supporting Information

Engineering a dual-site CuO/Cu_2O/CeO_2 heterostructure: synergistic Cu^+/Cu^{2+} and CeO_2 modulation for tandem ammonia electrosynthesis from nitrate

Junhua Li, Wenbiao Wang, Meiqing Cai, Ximin Zhang, Hui Qian, Xiaohui Xu, Xinjie Tian, Youbing Huang and Jun-Ling Song*

International Joint Research Center for Photoresponsive Molecules and Materials, School of Chemical and Material Engineering, Jiangnan University, Lihu Street 1800, Wuxi 214122, China

1 Experimental section

1.1 Materials and Chemicals

Commercial nickel foam (NF) was purchased from Suzhou Shengernuo Technology Co., LTD. Copper(II) nitrate trihydrate ($Cu(NO_3)_2 \cdot 3H_2O$, 99%), cerium(III) nitrate hexahydrate ($Ce(NO_3)_3 \cdot 6H_2O$, 99%), sodium nitrate ($NaNO_3$, 99%), urea (CH_4N_2O, 99%), sodium nitrite ($NaNO_2$, 99%), dipotassium hydrogen phosphate (K_2HPO_4,99%)， sodium nitrate-^{15}N ($Na^{15}NO_3$, ≥98.5%), 5,5-Dimethyl-1-pyrroline N-oxide (DMPO, 99%), ethanol (C_2H_5OH, 99.5%) were obtained from Shanghai Titan Technology Co., LTD or Sinopharm Chemical Reagent Co., LTD. Ammonium chloride (NH_4Cl), potassium dihydrogen phosphate (KH_2PO_4,99%), were purchased from Sinopharm Chemical Reagent Co., Ltd. Commercial NF was purc High-purity Ar (99.999%, gas) was purchased from Wuxi Liyuan Medical Oxygen Co., LTD. Deionized H_2O (18 MΩ) was utilized in all tests. All the chemical reagents were directly used as received without further purification.

2 Isotope labeling experiment

Isotope labeling was employed by replacing $Na^{14}NO_3$ with $Na^{15}NO_3$ for electrochemical reduction tests under identical conditions to identify the nitrogen source of ammonia in the products. After the reaction, H_2SO_4 was added to adjust the pH of the electrolyte to 2-3. 100 μL of the electrolyte was mixed with 500 μL DMSO-d_6 and 100 μL 3 M H_2SO_4 for subsequent ^{1}H-NMR analysis.

3 Electron paramagnetic resonance (EPR) analysis of H*

A typical three-electrode system was constructed in the H-type electrolytic cell, and the H* capture experiment was carried out with DMPO as the trapping agent in the constant potential electrolysis process. To ensure that a sufficient amount of H* is generated to obtain a clearly identifiable signal peak, the geometric area of the cathode electrode is set to 1 × 1 cm^2 NF loaded with the same molar amount of catalyst. 20 mM DMPO was added to the electrolyte and a constant flow of Ar was maintained throughout the process. After potentiostatically electrolyzing at -0.65 V vs. SCE for 10 minutes, a certain aliquot of the electrolyte was absorbed by a capillary tube for EPR detection.

4 Cathodic product analysis

The catholyte collected after the test was diluted to the quantification range of the calibration curve, and then different color reagents were added for the identification of NO_3RR products using UV-Vis spectrophotometry.

(1) Determination of ammonia-N

The NH_3 concentration in electrolytes after tests was quantitatively determined by Nessler's reagent. In a typical ammonia-N quantification procedure, 0.2 mL of electrolyte was taken out from the cathode chamber and diluted to 50 mL in the colorimetric tube. Then, Sodium potassium tartrate solution (2.4 M, 1 mL) and Nessler's reagent (1 mL) were added sequentially. After thoroughly shaking and standing for 20 minutes, the absorbance was tested by UV-Vis spectrophotometry at a wavelength of 420 nm. The concentration-absorption spectra were calibrated using standard NH_4Cl solution with different concentrations.

(2) Determination of nitrite-N

The NO_2^- concentration in electrolytes after tests was quantitatively determined by the Griess method. In a typical nitrite-N quantification procedure, 0.2 mL electrolyte was taken out from the cathode chamber and diluted to 50 mL in the colorimetric tube. 1 mL of color reagent was sequentially added. After thoroughly shaking and standing for 20 minutes, the absorbance at 540 nm was then measured by a UV-Vis spectrophotometer. The concentration-absorption spectra were calibrated using a standard $NaNO_2$ solution with different concentrations. The color reagent was prepared as follows: 20 g of p-amino benzenesulfonamide was dissolved in the mixed solution of water (250 mL) and phosphoric acid (50 ml). Then 1 g of N-(1-naphthyl)-ethylenediamine dihydrochloride was added to the above mixture. Finally, the above solution was diluted to 500 mL after being transferred to a volumetric flask.

(3) Determination of nitrate-N

Firstly, 0.2 mL electrolyte was taken out from the cathode cell and diluted to 50 mL in the colorimetric tube. Then, 1 mL 1 M HCl and 0.1mL 0.8 wt% sulfamic acid solution were added in turn into the aforementioned solution. Finally, the absorbance of the as-prepared mixture was detected by UV-Vis spectrophotometry at a wavelength of 220 nm and 275 nm. The corrected absorbance was calculated by the following equation: $A = A_{220\ nm} - 2A_{275\ nm}$. The concentration-absorption spectra were calibrated using standard KNO_3 solution with different concentrations.

(4) Calculation of the yield rate and the Faradaic efficiency of NH_3 and NO_2^-

The NH_3 yield rate = $(C_{NH3} \times V)/(t \times A)$

The Faradaic efficiency of NH_3 = $(8 \times F \times C_{NH3} \times V)/(17 \times Q) \times 100\%$

The NO_2^- yield rate = $(C_{NO2^-} \times V)/(t \times A)$

The Faradaic efficiency of NO_2^- = $(2 \times F \times C_{NO2^-} \times V)/(46 \times Q) \times 100\%$

Where C is the concentration of products, V is the volume of cathodic electrolyte, F is the Faraday constant (96485 C mol^{-1}), Q is the total charge passed through the system, t is the electrolysis time, and A is the geometric area of the working electrode.

5 Assembly of rechargeable Zn-nitrate batteries and electrochemical test

The prepared $CuO/Cu_2O/CeO_2$/NF electrocatalysts (1×1 cm^2) were employed as the cathode, and the polished Zn plates (2`×2 cm^2) worked as both reference and counter electrodes (anodes). A bipolar membrane (Fumasep FBM-PK) was employed as the separator to isolate the cathodic and anodic electrolytes in a typical H-cell. When constructing traditional rechargeable Zn-nitrate batteries, 20 mL of 1 M KOH aqueous solution with 0.02 M $Zn(CH_3COO)_2$ as an additive was introduced into the anodic side while another 20 mL of 1 M PBS solution with 100 mM $NaNO_3$ was added into the cathodic side. All electrochemical tests for Zn-nitrate batteries were conducted on a Chenhua CHI760e electrochemical workstation, with stirring rates of 400 rpm applied to both the anode and cathode during the tests. Discharge polarization profiles were obtained by conducting cathodic LSV from OCV to 0.005 V (vs. Zn^{2+}/Zn) with a scan rate of 5 mV/s and then the resultant power density curves could be figured out by P = I × V, where I and V are the discharge current density and voltage, respectively.

The electrochemical reactions during the discharge process of the rechargeable Zn-nitrate battery are presented as follows:

Cathode reaction: $NO_3^- + 7H_2O + 8e^- \rightarrow NH_4OH + 9OH^-$

Anode reaction: $4Zn + 8OH^- \rightarrow 4ZnO + 4H_2O + 8e^-$

Overall reaction: $4Zn + NO_3^- + 3H_2O \rightarrow 4ZnO + NH_4OH + OH^-$

The electrochemical reactions during the charging process of the rechargeable Zn-nitrate battery are presented as follows:

Cathode reaction: $4OH^- \rightarrow O_2 + 2H_2O + 4e^-$

Anode reaction: $2ZnO + 2H_2O + 4e^- \rightarrow 2Zn + 4OH^-$

Overall reaction: $2ZnO + 4OH^- \rightarrow O_2 + 2Zn$

6 In-situ ATR-FTIR measurements

In-situ ATR-FTIR was performed on the Thermo Scientific Nicolet iS50 spectrometer equipped with a liquid nitrogen-cooled MCT detector and a Si attenuated total reflection accessory. The ink of the catalyst was coated on a gold nanofilm as the working electrode, while SCE and platinum wire served as reference electrode and counter electrode. Potentiostatic tests were performed on a CHI 760E electrochemical workstation at the open-circuit potential and various potentials ranging from 0 V to −0.85 V vs. RHE. The background spectrum was acquired in the absence of applied potential. At each applied potential, FTIR spectra were recorded after holding the potential for approximately 30 seconds to allow current stabilization. And the spectra were obtained by averaging 32 scans at a resolution of 4 cm^{-1}.

7 Operando XAS

In this investigation, both static and in-situ X-ray absorption fine structure (XAFS) analyses of the Cu K-edge were conducted utilizing a commercial Laboratory-Based XAFS spectrometer (RapidXAFS 2M, Anhui Absorption Spectroscopy Analysis

Instrument Co., Ltd.). X-rays were generated via a Mo target X-ray source operated at 20 kV and 20 mA. A Si (553) spherically bent crystal analyzer (SBCA) with a radius of curvature of 500 mm served as the monochromator, thereby ensuring a diffraction geometry approaching a 90-degree backscatter angle at the absorption edge. After monochromatization, the X-rays pass through the sample and were collected using a high-energy-resolution silicon drift detector (SDD) to obtain the X-ray intensity. The XAFS data were acquired in transmission mode. During the XAFS measurements, the position of the absorption edge (E0) was calibrated using a standard Cu foil sample, and all data collection occurred within a single time period.

8 DFT calculation details

All calculations were performed within the framework of density functional theory (DFT) using the DMol³ module in Materials Studio, employing a plane-wave pseudopotential formalism. The exchange–correlation functional was described by the generalized gradient approximation (GGA) in the Perdew–Burke–Ernzerhof (PBE) parametrization. A double numerical basis set with polarization functions (DNP, version 4.4) was adopted to represent the electronic wavefunctions. Brillouin zone integration was carried out using a Γ-centered Monkhorst–Pack k-point mesh of 2×2×1. Structural relaxations utilized a Gaussian smearing scheme with a broadening width of 0.01 Ha, and the self-consistent Kohn–Sham iterations were converged to an energy tolerance of 1×10^{-5} Ha. All systems were treated with spin-polarized calculations to account for possible magnetic effects.

Three distinct heterointerface models were constructed and investigated: CuO–

Cu_2O, CuO–CeO_2, and Cu_2O–CeO_2. In these models, the CuO slab was cleaved along the (112) surface, the Cu_2O slab along the (110) surface, and the CeO_2 slab along the (111) surface, respectively. For the Gibbs free energy (ΔG) calculations of adsorption processes, zero-point energy (ΔZPE) and entropy corrections were included according to the relation:

$$\Delta G = \Delta E + \Delta ZPE - T\Delta S,$$

where ΔE is the ground-state electronic energy difference obtained from self-consistent DFT calculations, T=298.15 K is the standard temperature, and ΔS is the entropy change. The entropies of gas-phase molecules were taken from the NIST Chemistry WebBook database.

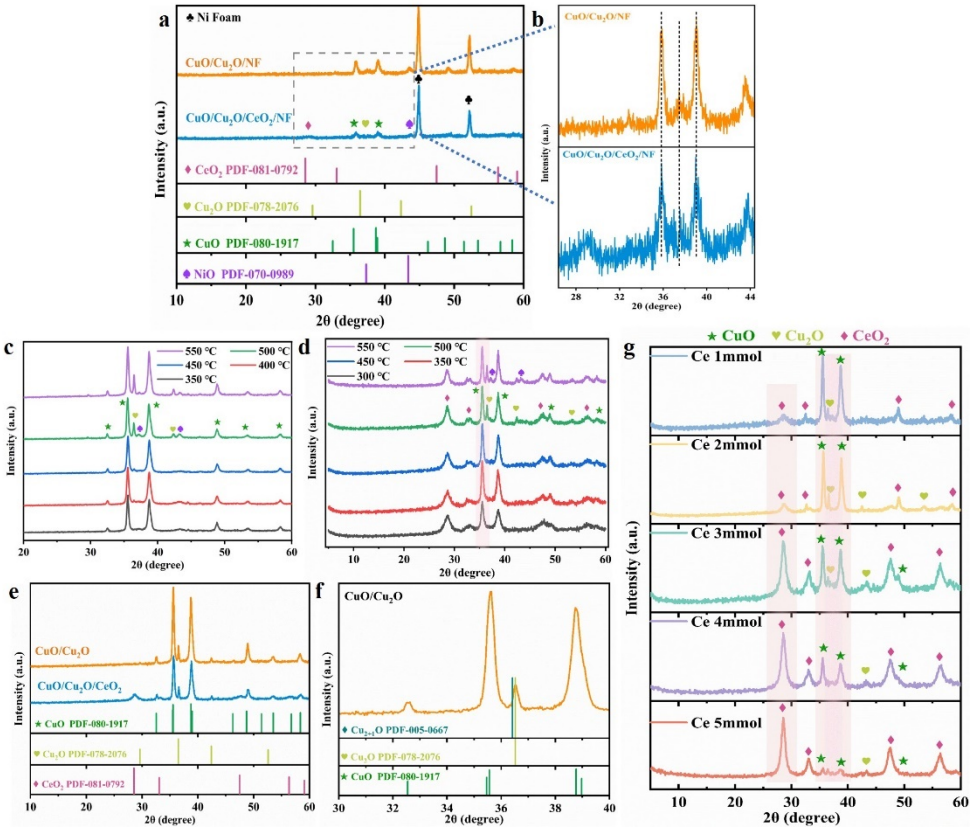

Fig. S1. (a-b) XRD pattern of the prepared $CuO/Cu_2O/NF$, $CuO/Cu_2O/CeO_2/NF$. (c) PXRD of CuHN/NF calcined at different temperatures (350/400/450/500/550 ℃); (d) PXRD patterns for the hydrothermal precursor after calcination at different temperatures (350, 400, 450, 500, and 550 °C); PXRD pattern of (e) the prepared CuO/Cu_2O, $CuO/Cu_2O/CeO_2$; (f) CuO/Cu_2O partial enlarged detail; (g) PXRD patterns of $CuO/Cu_2O/CeO_2$–x synthesized with different $Ce(NO_3)_3$ additions during the hydrothermal process. (Note: The powder catalyst for testing was scraped off from the nickel foam.).

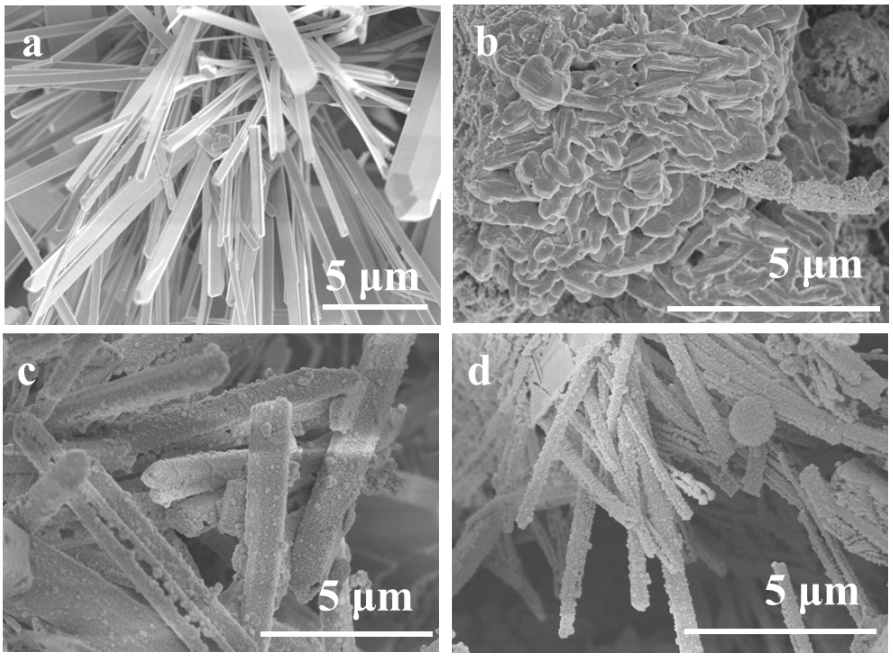

Fig. S2. SEM images of (a) CuHN/NF (b) $CuO/Cu_2O/NF$ (c) the corresponding hydrothermal precursor (d) $CuO/Cu_2O/CeO_2/NF$.

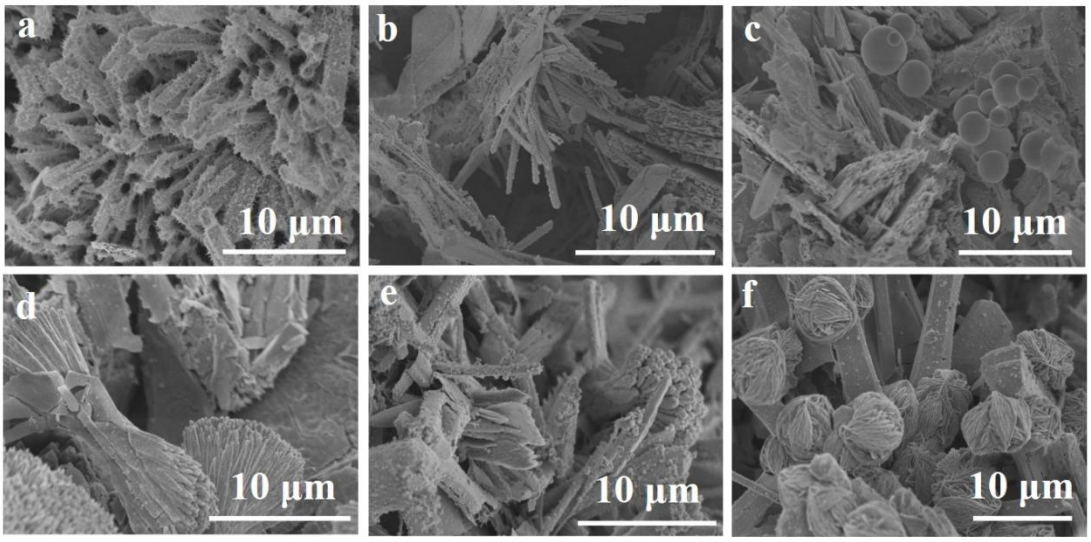

Fig. S3. SEM images of (a-f) $CuO/Cu_2O/CeO_2$/NF-*x* (*x*=1, 2, 3, 4, 5, 6)

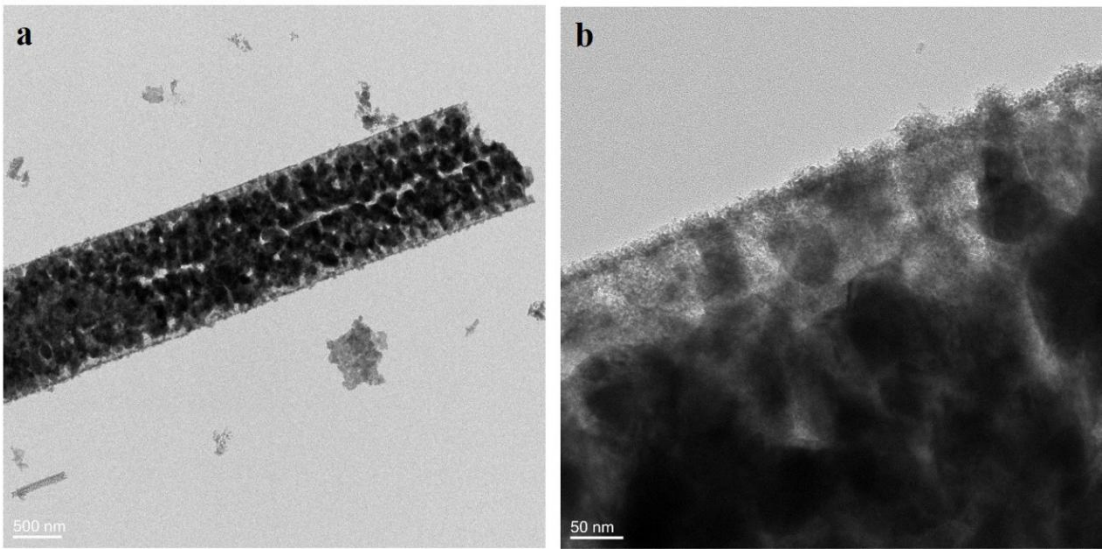

Fig. S4. TEM image and (d) HRTEM image of the prepared $CuO/Cu_2O/CeO_2$ electrocatalyst.

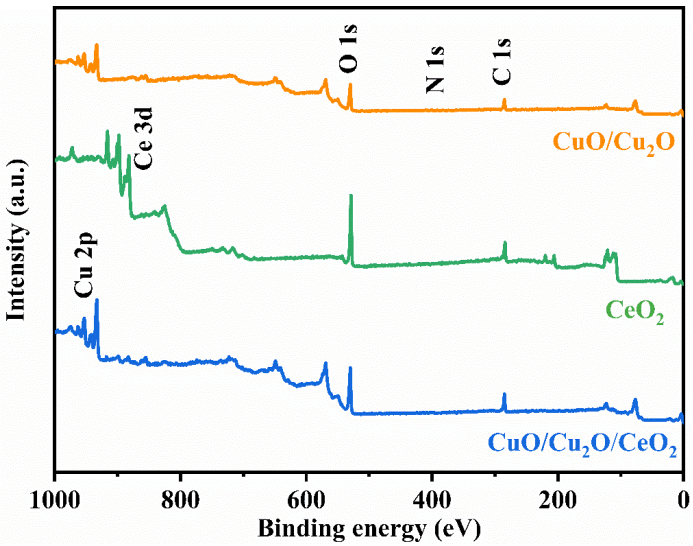

Fig. S5. Full XPS survey spectra of the synthesized electrocatalysts. (Note: The catalyst for testing was scraped off from the nickel foam.)

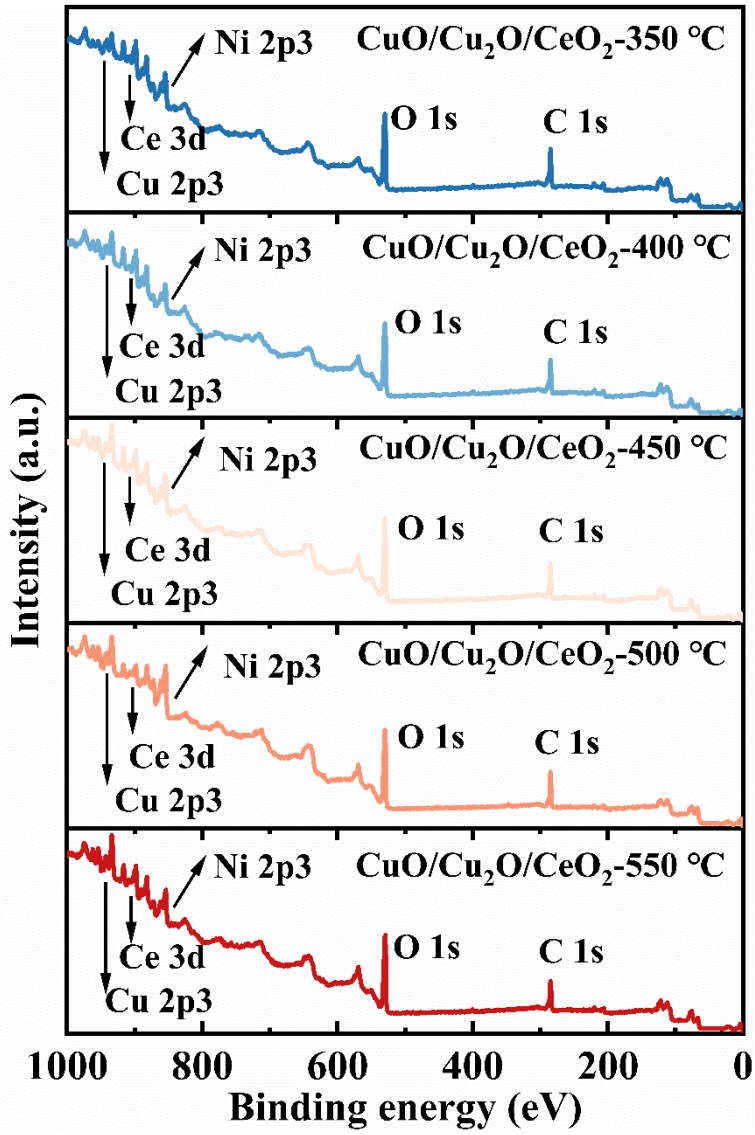

Fig. S6. Full XPS spectra of the catalysts calcined at different temperatures (Note: bulk measurements: tested with NF).

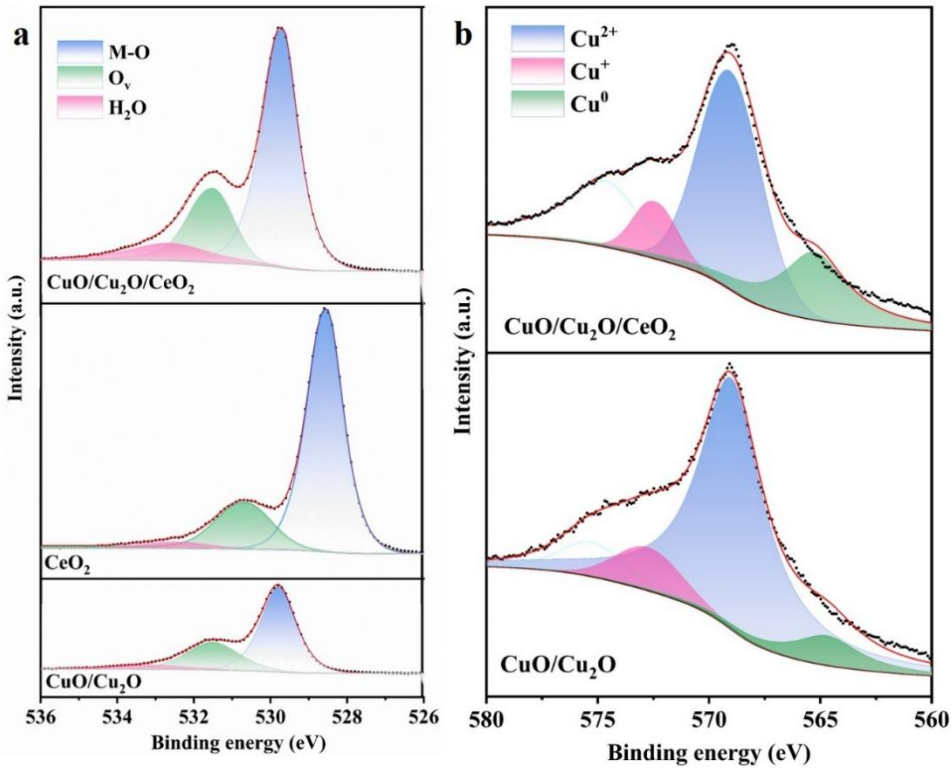

Fig. S7. High-resolution XPS spectra of the synthesized electrocatalysts: (a) O 1s; (b) Cu LMM Auger spectra. (Note: The catalyst for testing was scraped off from the nickel foam.)

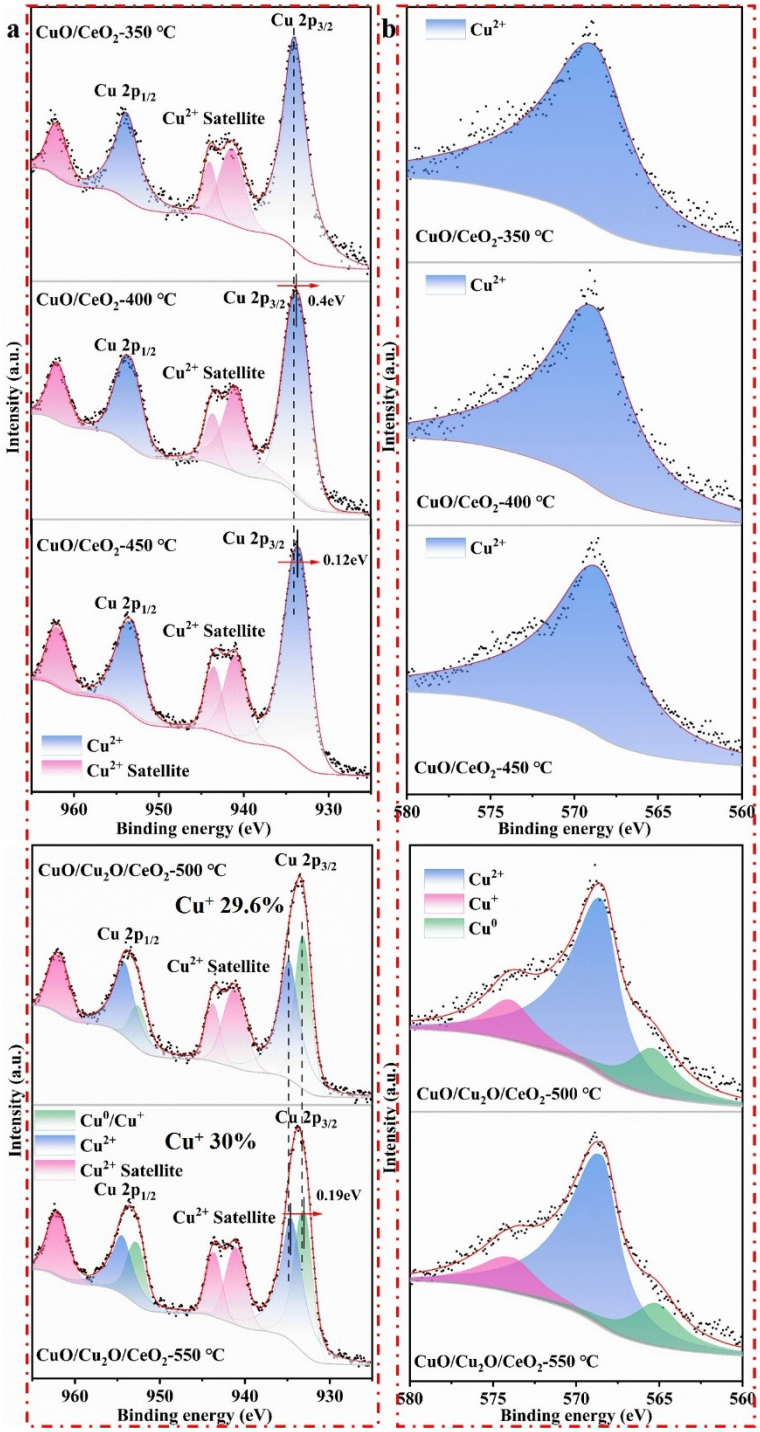

Figure S8. High-resolution XPS spectra of the synthesized electrocatalysts at different temperatures: (a) Cu 2p, (b) Cu LMM Auger spectra. (Note: bulk measurements: tested with NF.)

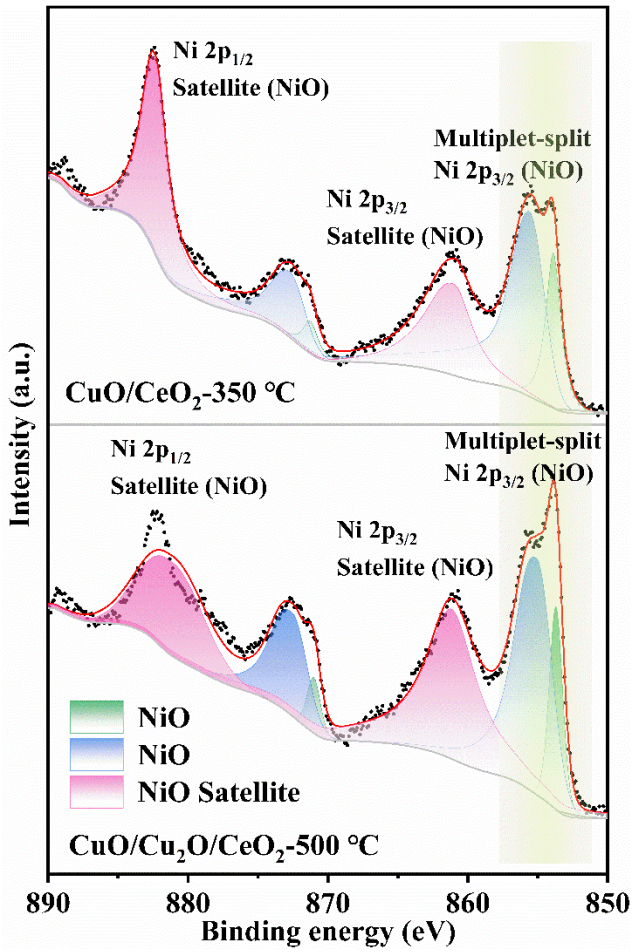

Figure S9. High-resolution Ni 2p XPS spectra of the synthesized electrocatalysts at different temperatures. (Note: bulk measurements: tested with NF.)

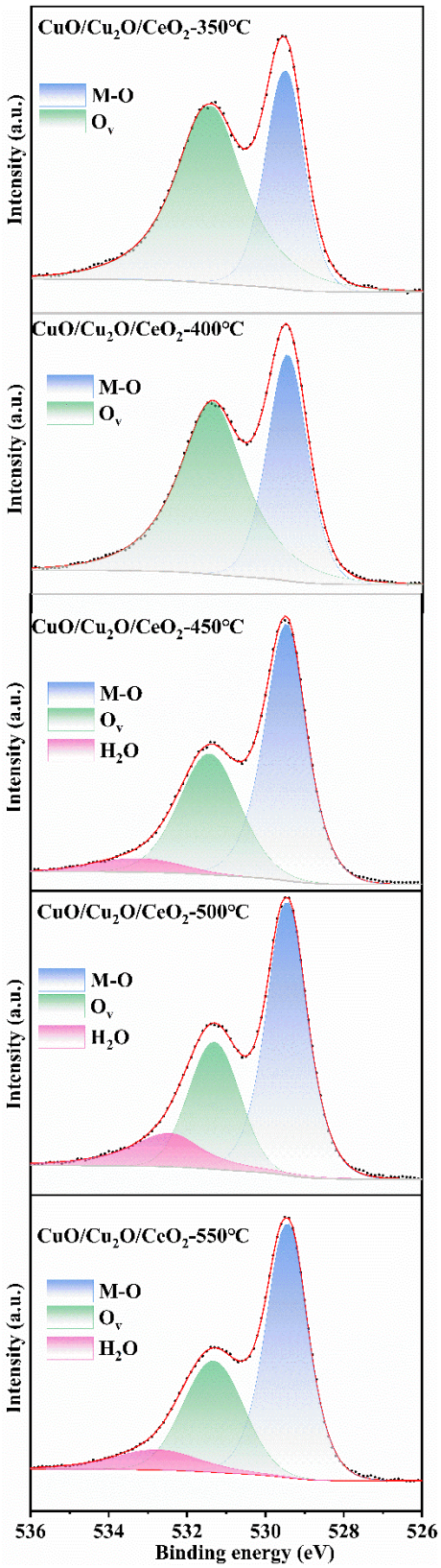

Figure S10. High-resolution O1s XPS spectra of the synthesized electrocatalysts at different temperatures. (Note: bulk measurements: tested with NF.)

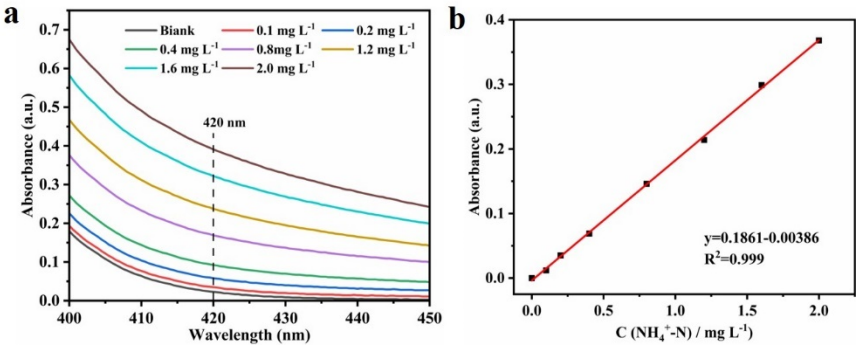

Fig. S11. (a) The UV-Vis absorption spectra and (b) the corresponding calibration curve of NH_4^+-N for different concentrations by using the Nessler method (Varying concentrations of NH_4^+-N are diluted in 50 mL colorimetric tubes for measurement).

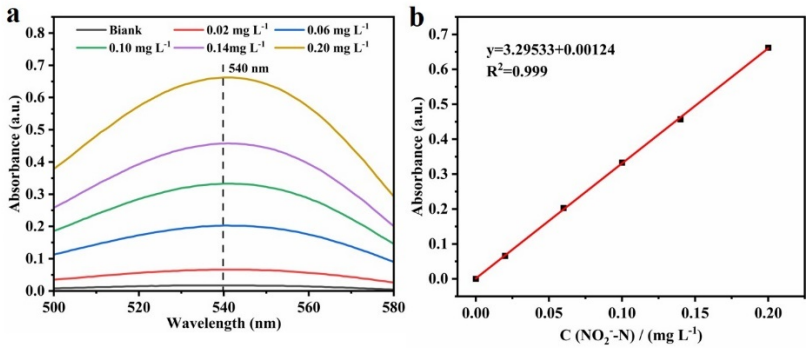

Fig. S12. (a) The UV-Vis absorption spectra and (b) the corresponding calibration curve of NO_2^--N for different concentrations by using the Griess method (Varying concentrations of NO_2^--N are diluted in 50 mL colorimetric tubes for measurement).

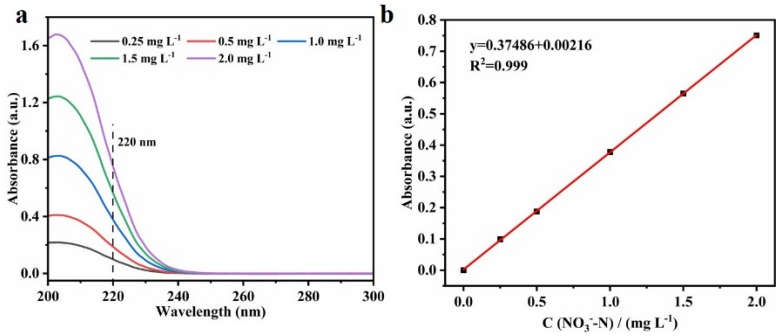

Fig. S13. (a) The UV-Vis absorption spectra and (b) the corresponding calibration curve of NO_3^--N for different concentrations (Varying concentrations of NO_3^--N are diluted in 50 mL colorimetric tubes for measurement).

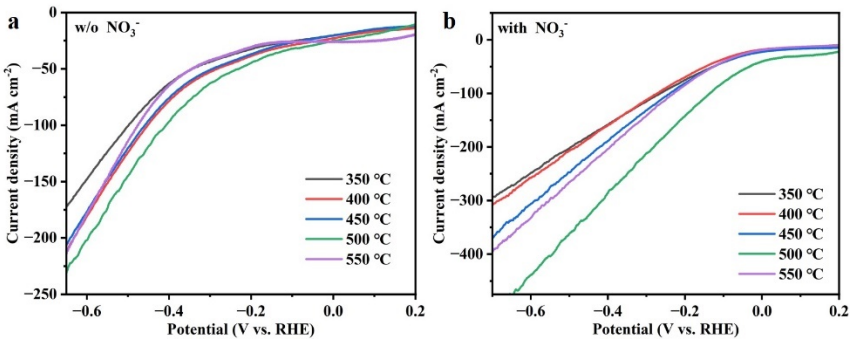

Fig. S14. The LSV curves of a series of materials, synthesized at different calcination temperatures, were recorded in electrolytes (a) w/o and (b)with NO_3^-. (Note: The hydrothermal precursor after calcination at different temperatures (350, 400, 450, 500, and 550 °C)

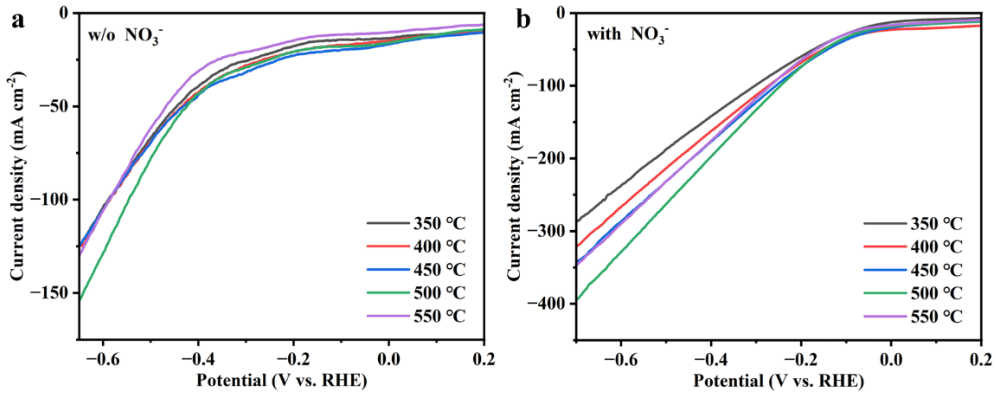

Fig. S15. The dependence of the reaction current density with NO_3^- on the Cu^+/Cu^{2+} ratio at various reaction temperatures. (Note: CuHN/NF calcined at different temperatures (350/400/450/500/550 °C.))

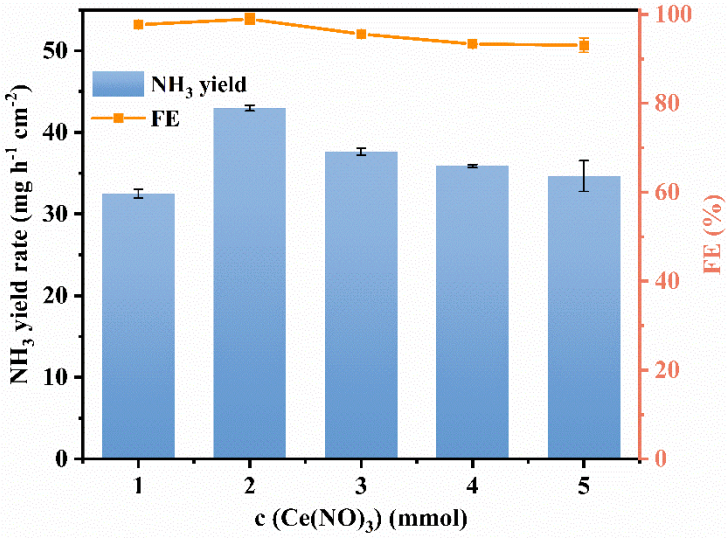

Fig. S16. The NH_3 yield of $CuO/Cu_2O/CeO_2$ using different concentrations $Ce(NO_3)_3$ in the hydrothermal process at −0.65 V vs. RHE. (Note: The catalyst was designated as $CuO/Cu_2O/CeO_2$/NF-*x* (*x* = 1,2,3,4,5).

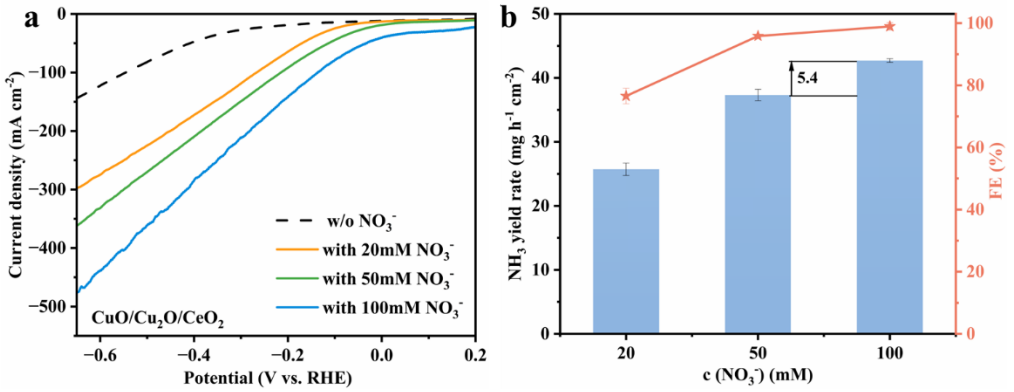

Fig. S17. (a) The LSV curves of $CuO/Cu_2O/CeO_2$ in the electrolyte containing different concentrations of NO_3^- and (b) corresponding NH_3 yield and FE at −0.65 V vs. RHE.

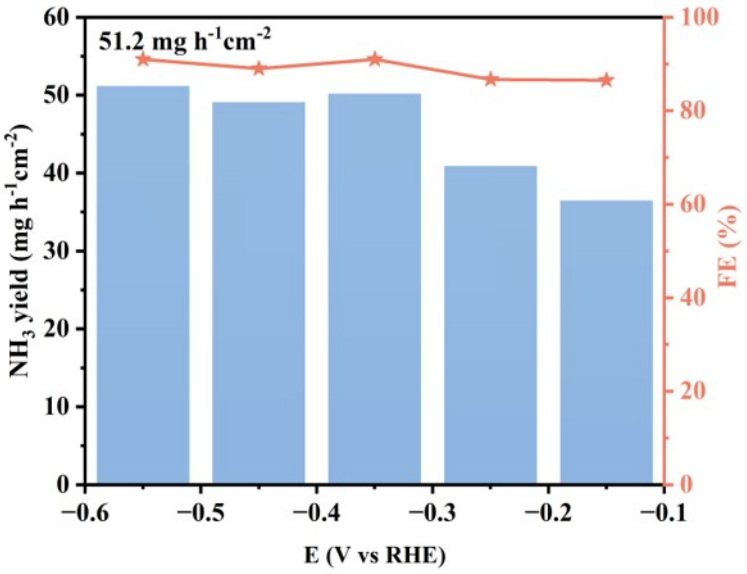

Fig. S18. NH_3 yield rates and FEs of $CuO/Cu_2O/CeO_2$ in neutral 1 M NaOH (pH 14) with 0.1 M NO_3^- at varying potentials.

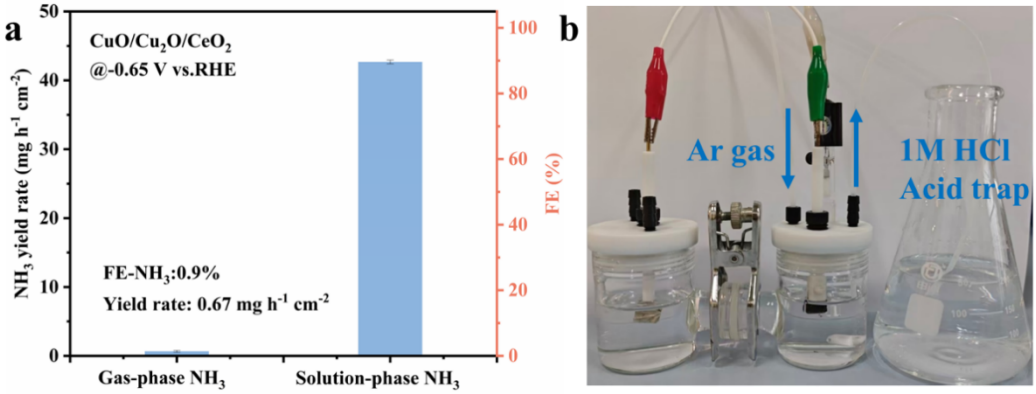

Fig. S19. (a) Gas-phase NH_3 production rate and corresponding FE of $CuO/Cu_2O/CeO_2$ at −0.65 V vs. RHE, as quantified through acid trap absorption. (b)Sealed H-cell electrolysis system integrated with 1 M HCl trap for capturing gaseous NH_3 products during NO_3RR.

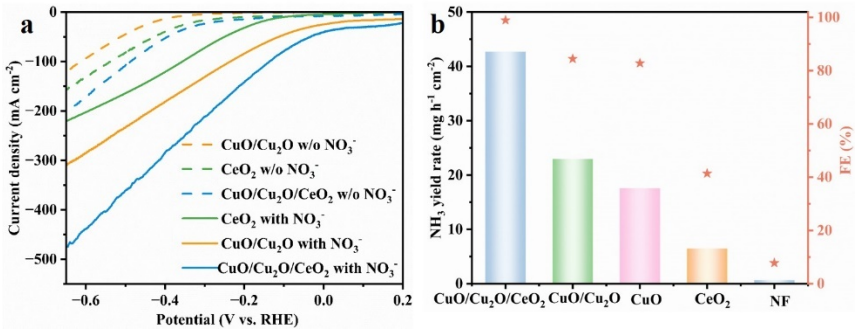

Fig. S20. (a) LSV curves of $CuO/Cu_2O/CeO_2$, CuO/Cu_2O, CeO_2, NF in 1 M PBS with or without 100 mM $NaNO_3$;(b) NH_3 yield and FE of $CuO/Cu_2O/CeO_2$, CuO/Cu_2O, CeO_2, CuO, and NF in 1 M PBS with 100 mM $NaNO_3$.

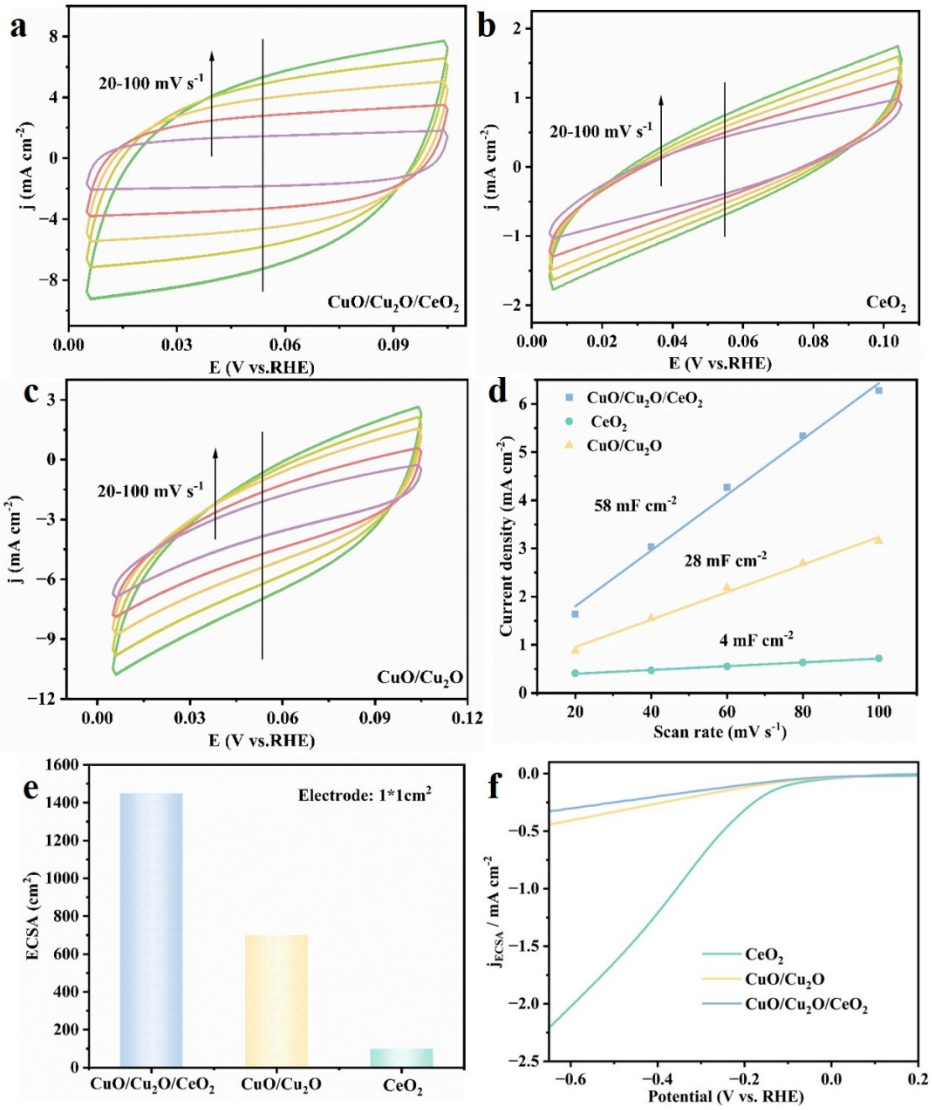

Fig. S21. CV curves of (a) $CuO/Cu_2O/CeO_2$, (b) CeO_2, (c) CuO/Cu_2O samples at different scan rates. CV curves of (d) C_{dl} of $CuO/Cu_2O/CeO_2$, CeO_2, and CuO/Cu_2O; (e) ECSA values of $CuO/Cu_2O/CeO_2$, CeO_2, and CuO/Cu_2O. (f) The linear-sweep voltammetry (LSV) curves of the electrocatalysts in this study normalized by electrochemically active surface area (ECSA).

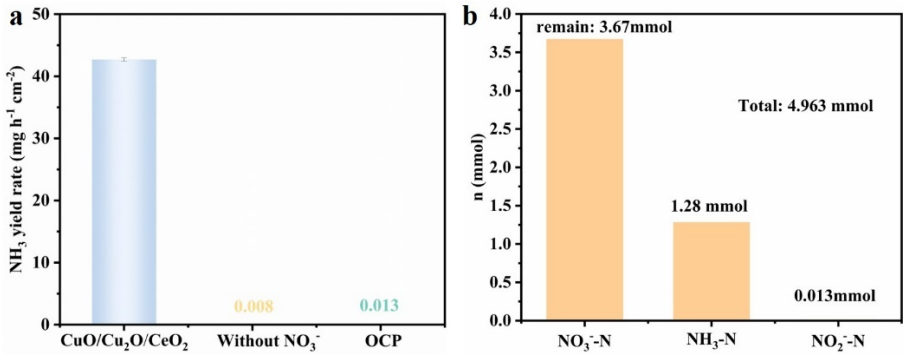

Fig. S22. (a) The NO_3RR performance of $CuO/Cu_2O/CeO_2$ with and without 100 mM NO_3^- at −0.65 V vs. RHE, and the NO_3RR performance of $CuO/Cu_2O/CeO_2$ with 100 mM NO_3^- at OCP; (b) Nitrogen Mass Balance Calculation.

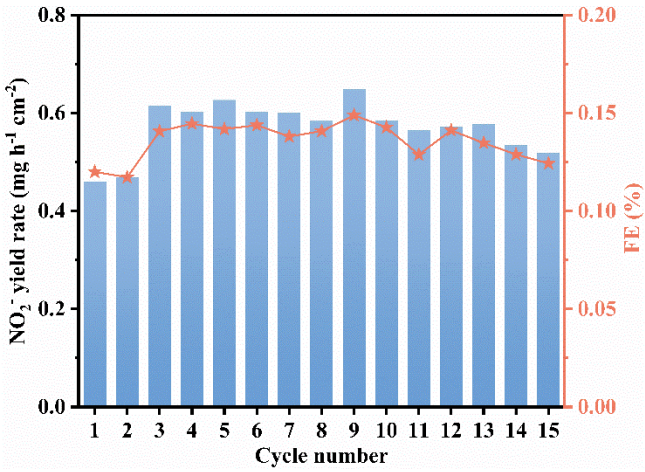

Fig. S23. Stability evaluation of $CuO/Cu_2O/CeO_2$ at -0.65 V (vs. RHE) for 1h: NO_2^- yield rates and FEs during 15 consecutive recycling tests.

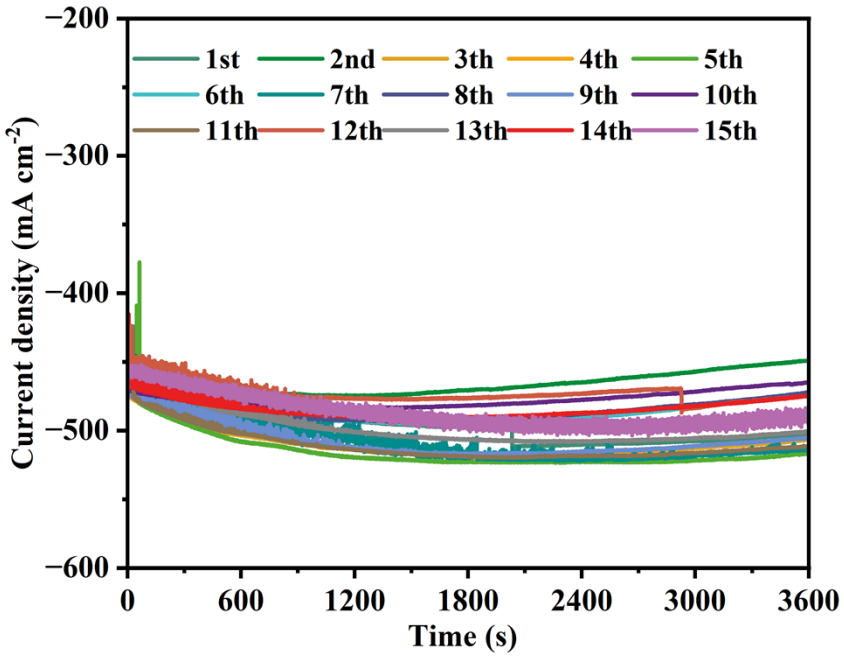

Fig. S24. The i-t curves of $CuO/Cu_2O/CeO_2$ at −0.65 V vs. RHE with 100 mM NO_3^- for 15-cycle stability test. (Note: 1 hour per cycle).

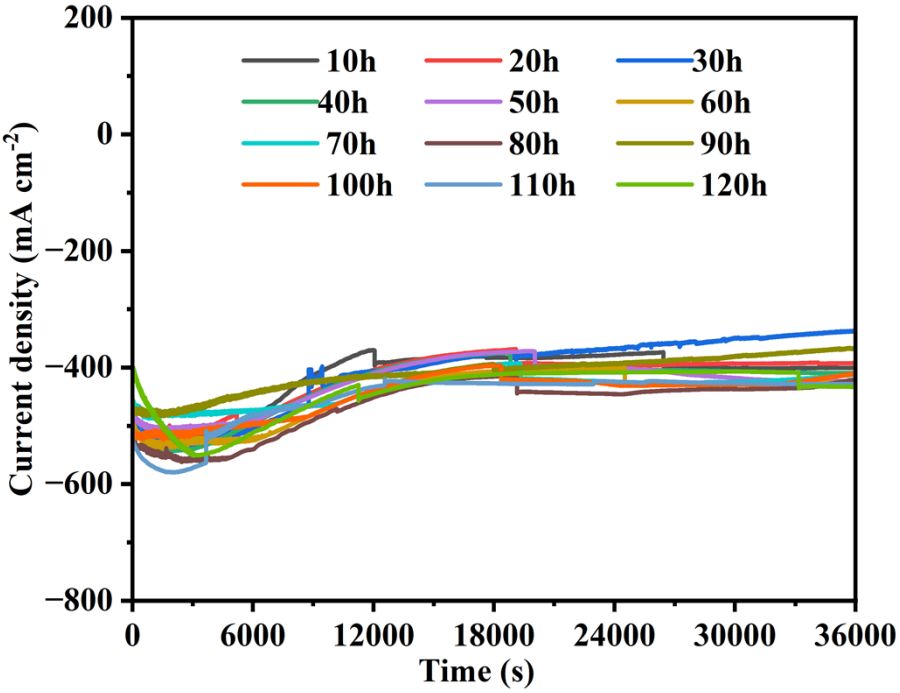

Fig. S25. The i-t curves of $CuO/Cu_2O/CeO_2$ at −0.65 V vs. RHE with 1000 mM NO_3^- for 120h stability test. (Note: 10 hour per cycle)

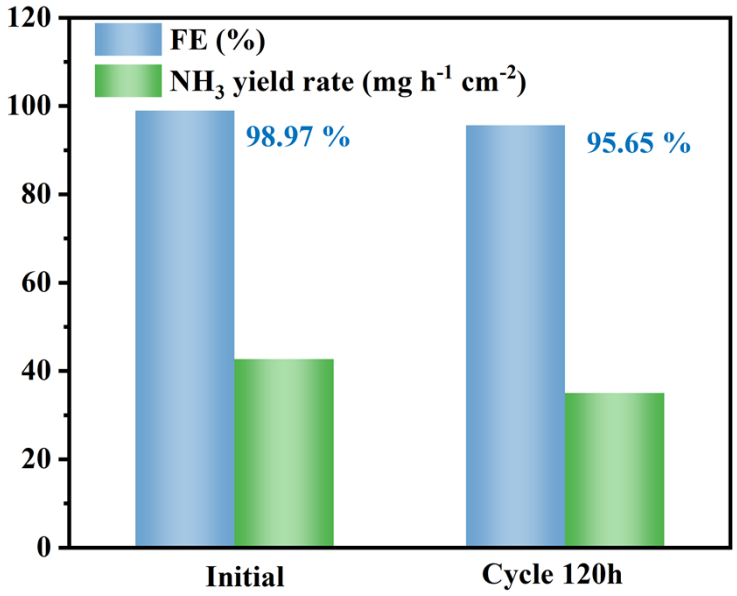

Fig. S26. Comparison of FE and NH_3 yield after 120 hours of cycling.

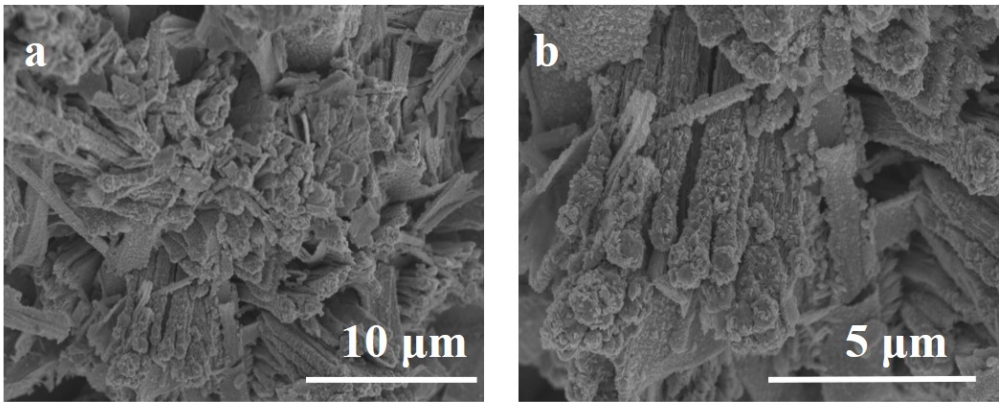

Fig. S27. SEM images of $CuO/Cu_2O/CeO_2$ electrocatalyst after NO_3RR stability testing.

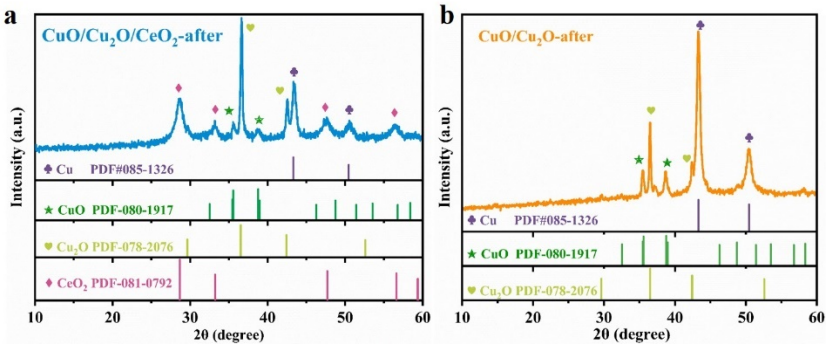

Fig. S28. PXRD pattern of $CuO/Cu_2O/CeO_2$ and CuO/Cu_2O electrocatalyst after NO_3RR stability testing. (Note: The powder catalyst for testing was scraped off from the nickel foam.)

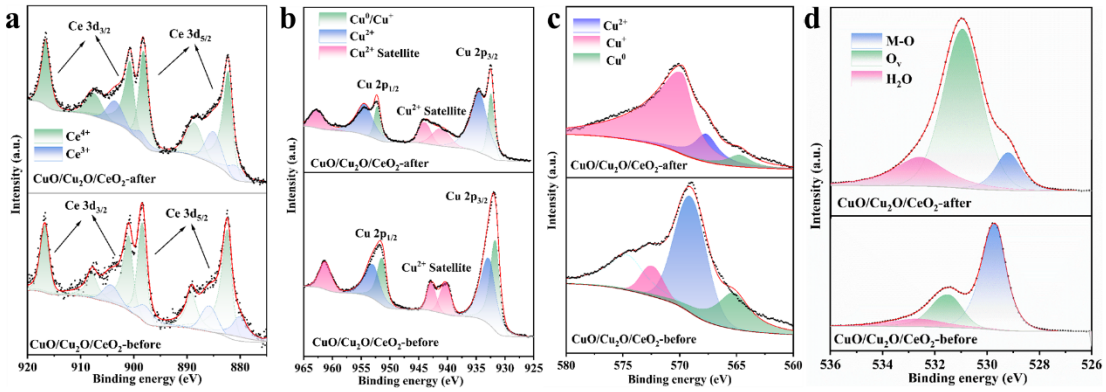

Fig. S29. The XPS spectra of $CuO/Cu_2O/CeO_2$ electrocatalyst after NO_3RR stability testing: (a) Ce 3d, (b) Cu 2p, and (c) Cu LMM Auger spectra. and (d) O 1s.

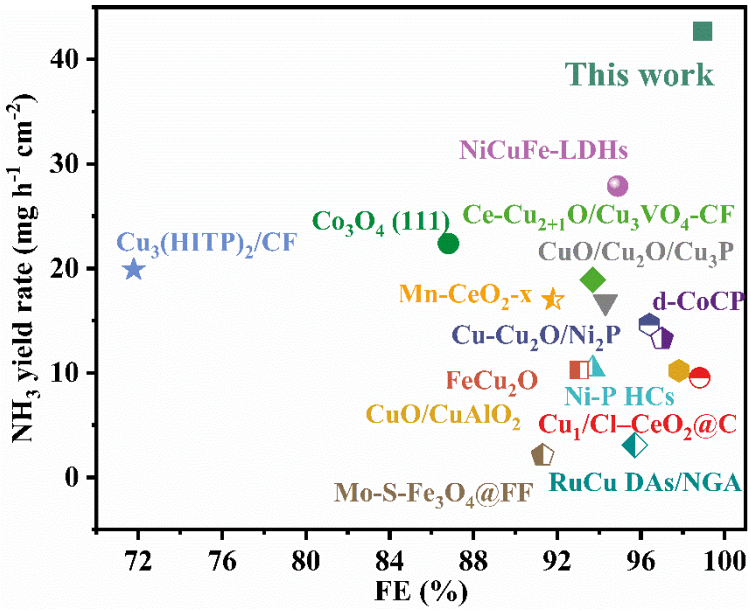

Fig. S30. Benchmarking of NH_3 yield rate for $CuO/Cu_2O/CeO_2$ electrocatalyst in this study at selected potentials against recent top-performing self-supporting electrocatalysts.

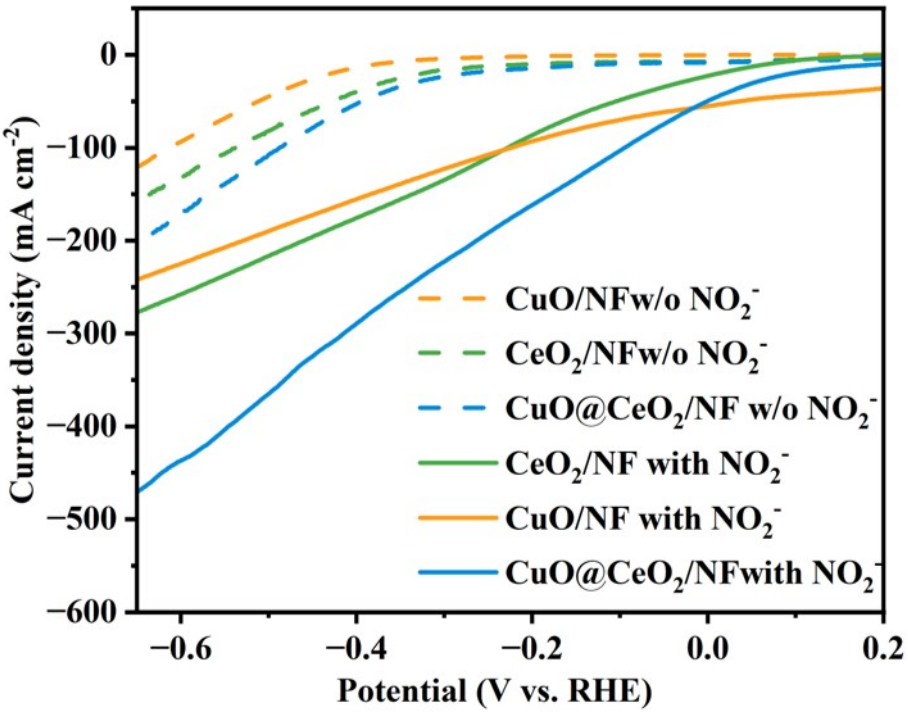

Fig. S31. (a) LSV curves of $CuO/Cu_2O/CeO_2$, CuO/Cu_2O, CeO_2 in 1 M PBS with or without 100 mM $NaNO_2$.

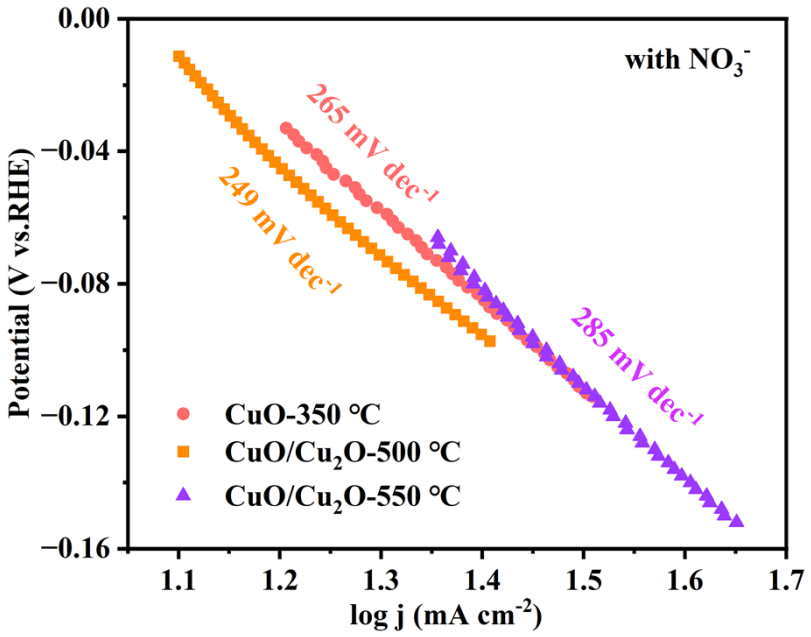

Fig. S32. (a) Tafel slopes of CuO-350 °C, CuO/Cu_2O-500 °C, and CuO/Cu_2O-550 °C in 1 M PBS with 100 mM NO_3^-.

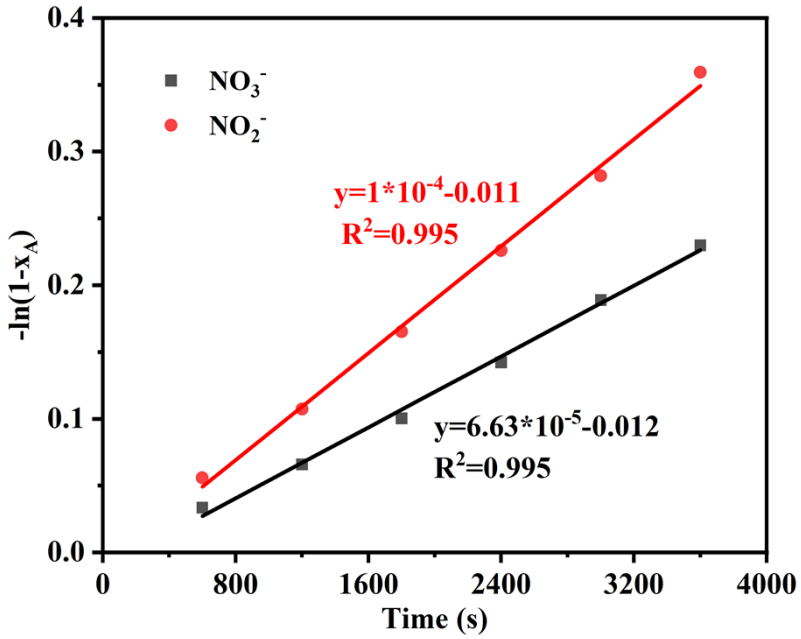

Fig. S33. Kinetic changes of NO_3^- and NO_2^- reduction to NH_3 for $CuO/Cu_2O/CeO_2$ in 1 M PBS with 100 mM $NaNO_3$ or 100 mM $NaNO_2$.

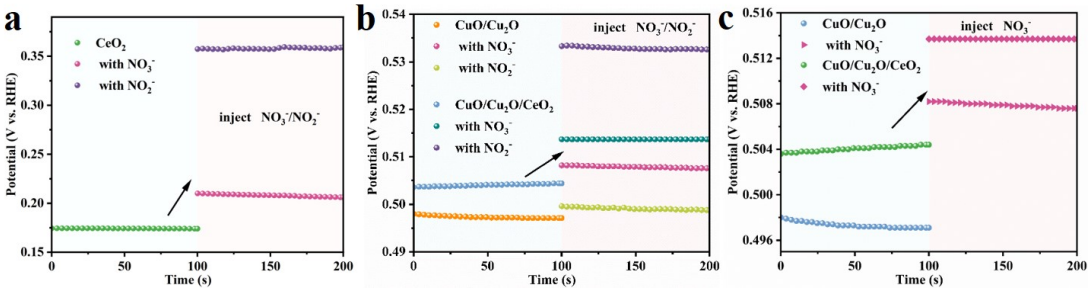

Fig. S34. The open-circuit potential of CeO_2, $CuO/Cu_2O/CeO_2$ and CuO/Cu_2O in 1M PBS with/without 100 mM NO_3^-/ NO_2^-.

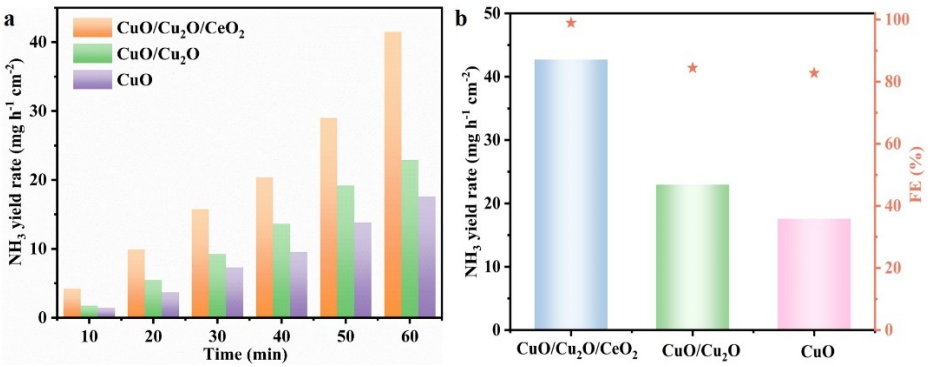

Fig. S35. (a) Variation of NH_3 yield with electrocatalytic reduction time at -0.65V vs. RHE potentials; (b) NH_3 yield rate, and FE of $CuO/Cu_2O/CeO_2$, CuO/Cu_2O and CuO at -0.65V vs. RHE potentials after 1 h.

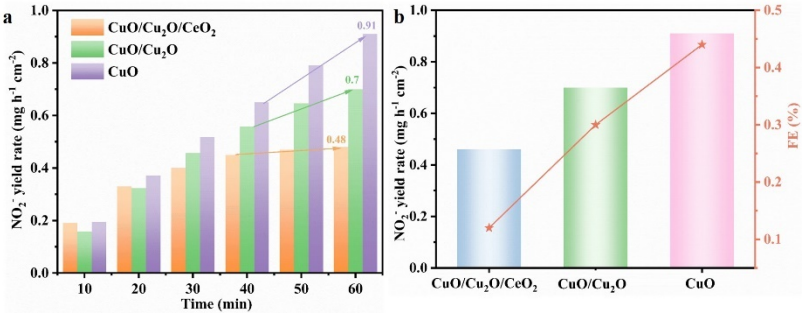

Fig. S36. (a) Variation of NO_2^- yield with electrocatalytic reduction time at -0.65V vs. RHE potentials; (b) NO_2^- yield rate, and FE of $CuO/Cu_2O/CeO_2$, CuO/Cu_2O and CuO at -0.65V vs. RHE potentials after 1 h.

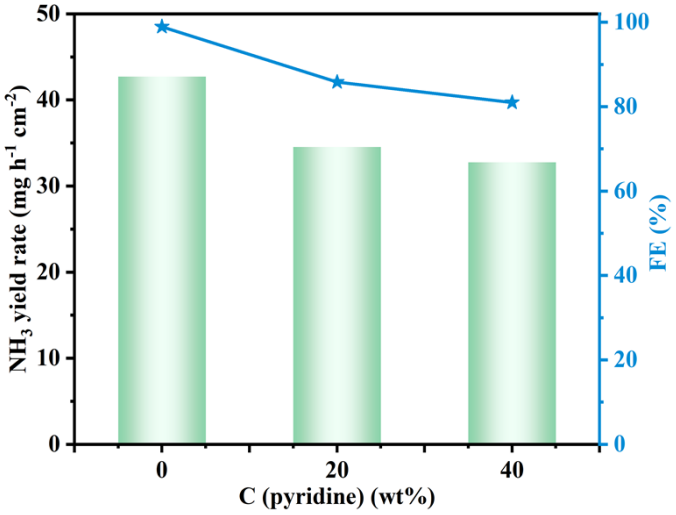

Fig. S37. The NH_3 yield rate and FE of $CuO/Cu_2O/CeO_2$ at −0.65 V vs. RHE after adding different concentrations of pyridine.

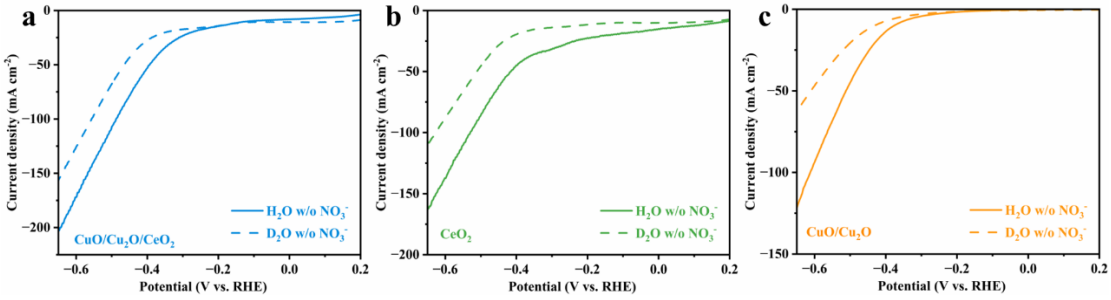

Fig. S38. LSV profiles of $CuO/Cu_2O/CeO_2$, CeO_2, and CuO/Cu_2O in 1 M PBS aqueous solutions prepared with and without H_2O or D_2O.

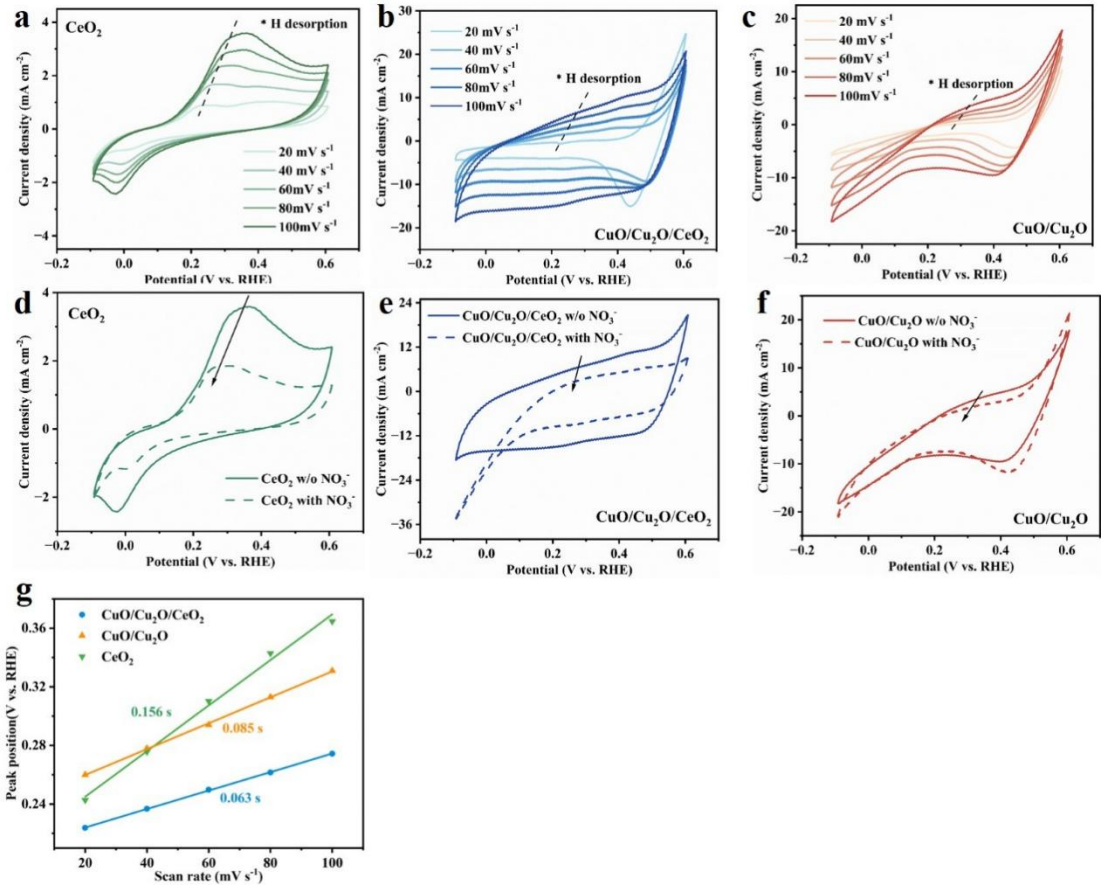

Fig. S39. CV curves of (a) CeO_2, (b) $CuO/Cu_2O/CeO_2$, and (c) CuO/Cu_2O in 1 M PBS under different scan rates. CV curves of (d) CeO_2, (e) $CuO/Cu_2O/CeO_2$, and (f) CuO/Cu_2O in 1 M PBS with 100 mM NO_3^-. (g) *H desorption kinetic plots of CeO_2, $CuO/Cu_2O/CeO_2$, and CuO/Cu_2O.

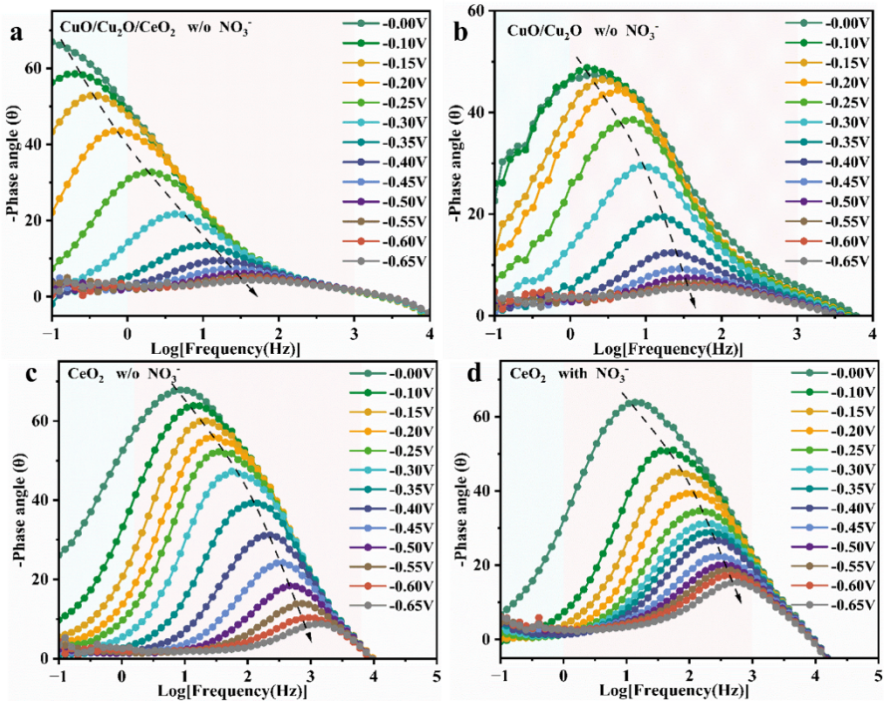

Fig. S40. Bode phase plots for (a) $CuO/Cu_2O/CeO_2$ (b) CuO/Cu_2O and (c) CeO_2 in 1 M PBS without 100 mM NO_3^- under varied potentials, and for (d) CeO_2 in 1 M PBS with 100 mM NO_3^- under varied potentials.

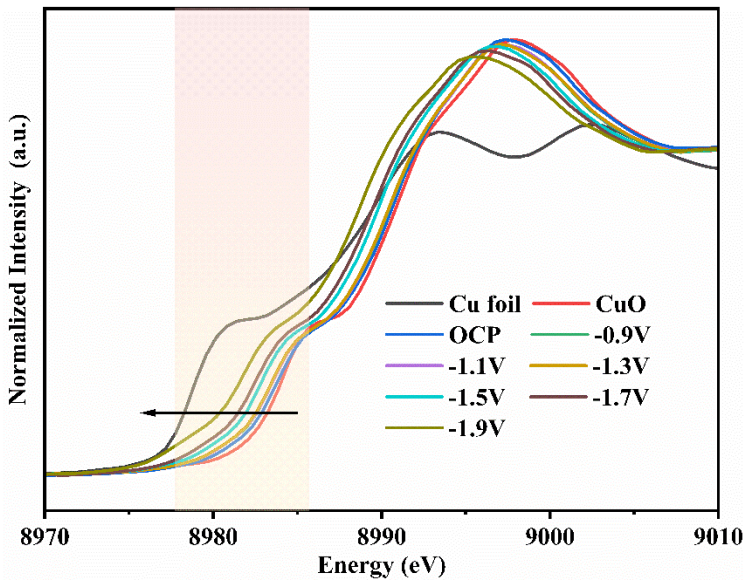

Fig. S41. XANES spectra of $CuO/Cu_2O/CeO_2$ at different potentials in 1 M PBS containing 0.1 M NO_3^-.

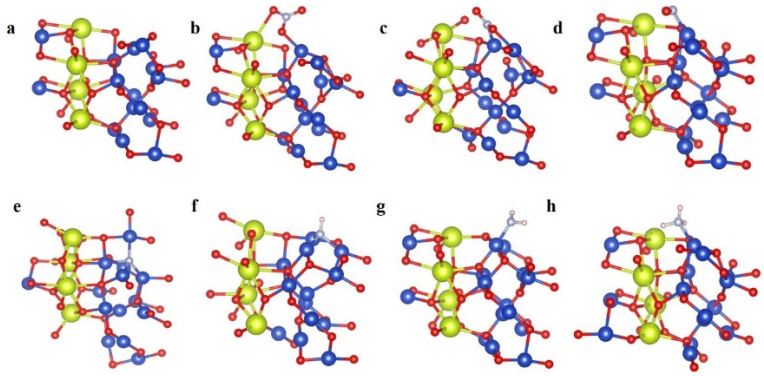

Fig. S42. The corresponding adsorption configurations of NO_3RR reduction intermediates on the Cu_2O/CeO_2 catalyst.

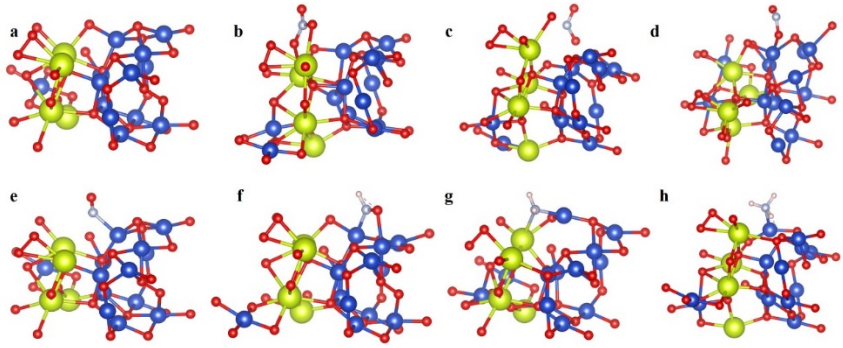

Fig. S43. The corresponding adsorption configurations of NO_3RR reduction intermediates on the CuO/CeO_2 catalyst.

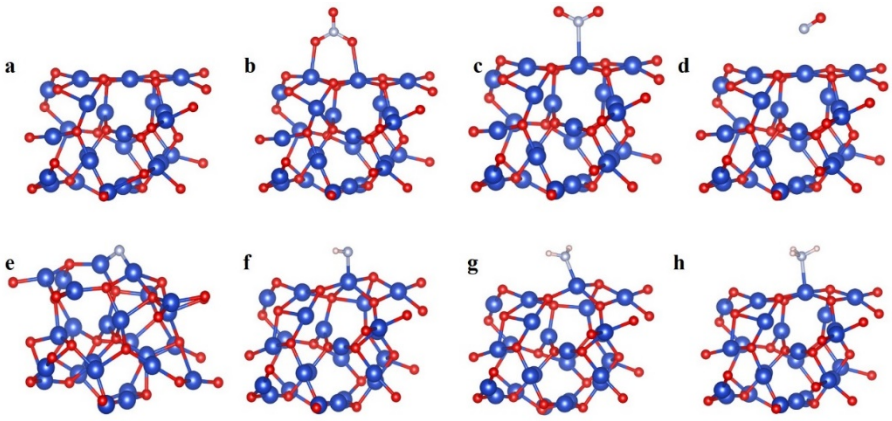

Fig. S44. The corresponding adsorption configurations of NO_3RR reduction intermediates on the CuO/Cu_2O catalyst.

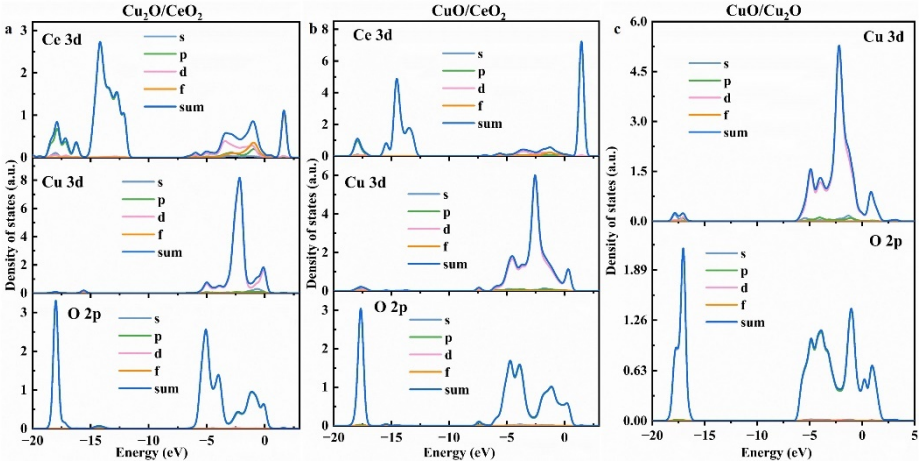

Fig. S45. The pDOS of Cu_2O/CeO_2, CuO/CeO_2, and CuO/Cu_2O, respectively.

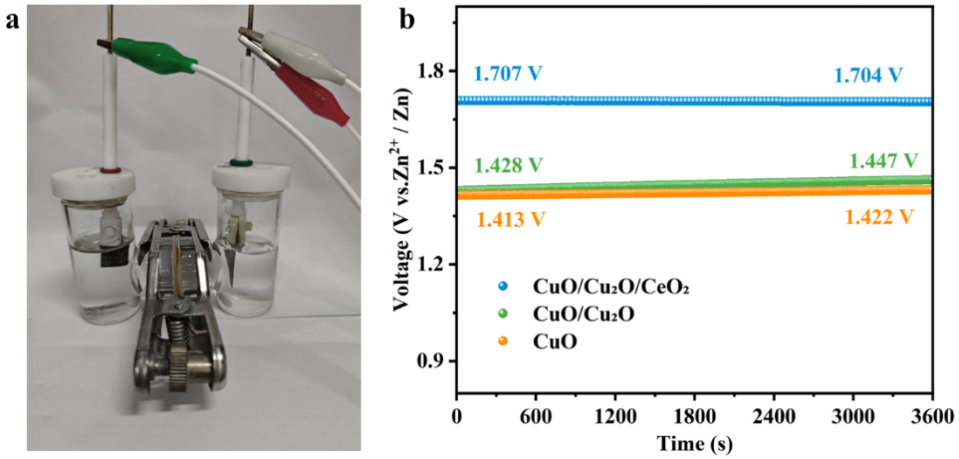

Fig. S46. (a) Device structure of the Zn-NO_3^- battery; **(**b) The OCP profiles of rechargeable Zn-NO_3^- batteries over 1 hour.

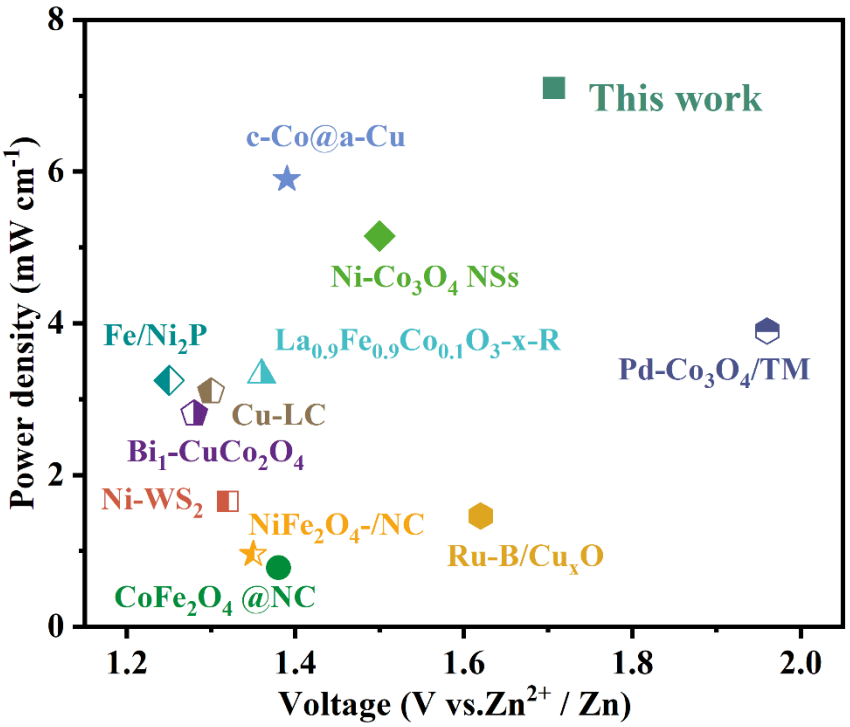

Fig. S47. Comparative performance of the $CuO/Cu_2O/CeO_2$-based Zn-NO_3^- battery against prior studies.

Table S1. The specific binding energy positions of the corresponding peaks after XPS peak fitting for $CuO/Cu_2O/CeO_2$, CeO_2 and CuO/Cu_2O (Note: The powder catalyst for testing was scraped off from the nickel foam.).

Binding energy (eV)	Cu^{2+} $2p_{3/2}$	$Cu^{1+/0}$ $2p_{3/2}$	Ce^{3+} $3d_{5/2}$	Ce^{4+} $3d_{5/2}$
$CuO/Cu_2O/CeO_2$	932.76	931.62	885.83	889.18
CeO_2	—	—	885.13	888.78
CuO/Cu_2O	933.83	932.62	—	—

Table S2. Comparison of NH_3 yield rate and Faradic efficiency (FE) of reported self-supporting catalysts.

Catalyst (Self-supporting)	Electrolyte	Potential (V vs. RHE)	NH_3 yield rate @Potential ($mg\ h^{-1}\ cm^{-2}$)	FE @Potential (%)	Ref.
$CuO/Cu_2O/CeO_2$	1 M PBS (0.1 M $NaNO_3$)	−0.65 V	43.37	99.85	This work
$CuO/Cu_2O/CeO_2$	1 M KOH (0.1 M $NaNO_3$)	−0.65 V	51.2	90	This work
Co_3O_4 (111)	1 M KOH (0.1 M NO_3^-)	-0.9 V	22.38	86.8	1
$CuO/CuAlO_2$	0.1 M PBS (0.1 M NO_3^-)	-1.0 V	10.21	97.81	2
Mn-CeO_2−x	1 M KOH (0.1 M NO_3^-)	-0.6 V	17.01	91.8	3
Ce-$Cu_{2+1}O/Cu_3VO_4$-CF	1 M KOH (0.1 M NO_3^-)	-0.5 V	18.905	93.7	4
Ni-P HCs	0.5 M Na_2SO_4 (0.1 M NO_3^-)	-0.8 V	10.37	93.7	5
RuCu DAs/NGA	0.1 M KOH (0.1 M NO_3^-)	-0.4 V	3.1	95.7	6
Cu-Cu_2O/Ni_2P	0.1 M PBS (0.1 M NO_3^-)	-1.0 V	14.636	96.4	7
$Cu_3(HITP)_2$/CF	1 M KOH (0.1 M NO_3^-)	-0.9 V	19.9	71.78	8
d-CoCP	1 M KOH (0.1 M NO_3^-)	-0.5 V	13.26	97.0	9
Mo-S-Fe_3O_4@FF (Foam iron)	0.1 M K_2SO_4 (0.1 M NO_3^-)	-1.3 V	2.1	91.30	10

$FeCu_2O$	1 M KOH (0.1 M KNO_3)	-0.3 V	10.27	93.05	11
$CuO/Cu_2O/Cu_3P$	0.1 M KOH (0.1 M NO_3^-)	-0.8 V	16.8	94.3	12
$Cu_1/Cl–CeO_2@C$	0.5 M Na_2SO_4 (0.1 M KNO_3)	-0.5 V	9.528	98.8	13
NiCuFe-LDHs	1 M KOH (0.1 M $NaNO_3$)	-0.4 V	27.88	94.8	14

Table S3. Performance benchmarking of $CuO/Cu_2O/CeO_2$ in NO_3RR against state-of-the-art heterojunction catalysts with BIEF or hydrogen spillover effects.

Catalyst (Heterojunction)	NH_3 yield rate (mg h^{-1} cm^{-2})	FE-NH_3 (%)	Initial potential (V vs. RHE)	Cycle hours	Tafel Slope (mV dec^{-1})	Ref.
$CuO/Cu_2O/CeO_2$	43.37	99.85	−0.65	120	166	This work
$Cu/Cu_{2+1}O$@PANI	4.83	90.89	-0.7	5	289	15
Cu-CoP	7.56	85.1	−1.0	84	102	16
Ni−P HCs	10.37	93.7	-0.8	25	251	5
Mo-S-Fe_3O_4@FF	2.1	91.3	−1.3	20	63.7	10
Cu_{SA}NPC	2.6	87.2	−1.1	10	229	17
Pd@Cu-1.35%	21	97	−0.8	15	91	18

Table S4. Lists the Gibbs free energy changes for each elementary step on the three catalysts.

Elementary step	Cu_2O/CeO_2	CuO/CeO_2	CuO/Cu_2O
$*NO_3$	-2.59	-2.45	−1.74
$*NO_2$	-4.58	-3.92	-3.51
*NO	-5.73	-5.57	−5.22
*N	-5.38	-6.75	-5.92
*NH	-7.21	-6.52	−4.78
$*NH_2$	-7.62	-7.32	−6.9
$*NH_3$	-8.37	-8.17	−8.18
*	-8.46	-8.46	-8.46

Table S5. The performance comparison of our proposed $CuO/Cu_2O/CeO_2$ based Zn-NO_3^- battery with other reported works.

Catalyst	Anolyte	Catholyte	OCV (V vs. Zn_2^+/Zn)	Power density (mW cm^{-2})	Ref.
$CuO/Cu_2O/CeO_2$	1 M KOH (0.02 M $Zn(CH_3COO)_2$)	1 M PBS (0.1 M $NaNO_3$)	1.707	7.10	This work
$CoFe_2O_4$@NC	3 M KOH (0.5 M $Zn(CH_3COO)_2$)	1 M KOH (0.1 M KNO_3)	1.38	0.78	19
Ru—B/Cu_xO	0.1 M KOH	0.1 M KOH (0.1 M KNO_3)	1.62	1.46	20
$NiFe_2O_4$/NC	6 M KOH	1 M KOH (0.1 M KNO_3)	1.35	0.96	21
Ni-Co_3O_4 NSs	0.1 M KOH (0.1 M HMF)	1 M K_2SO_4 (0.1 M KNO_3)	1.50	5.15	22
$La_{0.9}Fe_{0.9}Co_{0.1}O_3$-x-R	1 M KOH	1 M KOH (0.5 M KNO_3)	1.36	3.32	23
Fe/Ni_2P	1 M KOH	0.2 M K_2SO_4 (0.05 M KNO_3)	1.25	3.25	24
Pd-Co_3O_4/TM	1 M KOH	0.1 M KOH (0.1 M KNO_3)	1.96	3.9	25

c-Co@a-Cu	1 M KOH	0.1 M Na_2SO_4 (0.05 M $NaNO_3$)	1.39	5.9	[26]
Bi_1-$CuCo_2O_4$	1 M NaOH	0.5 M Na_2SO_4 (0.1 M $NaNO_3$)	1.28	2.81	[27]
Cu-LC	1 M KOH	0.5 M Na_2SO_4 (4500 ppm $NaNO_3$)	1.30	3.1	[28]
Ni-WS_2	1 M KOH	1 M KOH (0.1 M KNO_3)	1.32	1.65	[29]

Reference

1 Y. Sun, Y. X. Shi, Y. H. Gao, M. L. Sun, Y. B. Yao, H. W. Yu, Y. Xu, X. Wang and Y. J. Yang, *Chem. Eng. J.*, 2025, **512**, 162506.

2 M. Zhang, X. Cheng, Y. Duan, J. Chen, L. Wang and Y. Q. Wang, *Adv. Funct. Mater.*, 2024, **35**.

3 X. T. Sun, W. T. Rong, L. F. Wang, J. N. Lv, R. X. Yang, T. T. Liang, Q. W. Yang, X. H. Xu and Y. Liu, *Chem. Eng. J.*, 2025, **512**, 162323.

4 M. Zhang, Y. Liu, Y. Duan, X. Liu and Y. Q. Wang, *J. Colloid Interface Sci.*, 2024, **671**, 258-269.

5 Q. Hu, C. Y. Shang, X. B. Chen, S. Qi, Q. H. Huo, H. P. Yang and C. X. He, *J. Am. Chem. Soc.*, 2025, **147**, 12228-12238.

6 K. Y. Liu, Z. Y. Sun, X. J. Peng, X. D. Liu, X. Zhang, B. R. Zhou, K. D. Yu, Z. B. Chen, Q. Zhou, F. Zhang, Y. Wang, X. Gao, W. X. Chen and P. W. Chen, *Nat. Commun.*, 2025, **16**, 2167.

7 H. L. Zhao, P. F. Liu, X. T. Cheng, C. Fan, J. Liu, D. X. Kan and Y. Q. Wang, *Adv. Funct. Mater.*, 2025, **35**, 202425459.

8 W. Wang, B. Chen, J. Guo, Z. Liu, H. Yuan, B. Fan and X. Huang, *Adv. Funct.*

Mater., 2025, **35**.

9 Y. D. Ding, S. H. Zhang, Y. X. Liu, Y. Liu, H. Zheng, L. Qing, Y. H. Song, Z. W. Ma, L. S. Zhang and T. X. Liu, *Adv. Funct. Mater.*, 2025, **35**, 202422339.

10 M. N. Ran and G. Zhang, *Chem. Eng. J.*, 2025, **516**, 164104.

11 J. L. Wei, J. L. Wang, W. Q. Yu, J. W. Li, Y. Yang, Y. P. Wang, N. Li, R. D. Xu, L. J. Yang, G. X. Li and P. J. Dyson, *Appl. Catal. B: Environ. Energy*, 2025, **378**, 125629.

12 R. Han, R. Hu, H. Zhao, P. Liu and Y.-Q. Wang, *Chem. Eng. J.*, 2025, **520**.

13 S. Y. Wang, X. Ji, S. C. Wang, P. Jing, X. Xu, B. C. Liu and J. Zhang, *Adv. Funct. Mater.*, 2025, **35**, 202502073.

14 B. Liu, Y. Wang, H. Wen, Y. Wang, H. Liu, B. Da, K. Li, H. Luo, H. Li and K. Yan, *Adv. Funct. Mater.*, 2025, DOI: 10.1002/adfm.202519238.

15 C. Z. Sun, Q. Zhao, Y. G. Xiao, X. Liu, X. H. Yuan and S. S. Cao, *Chem. Eng. J.*, 2025, **519**, 165200.

16 W. H. Yang, Z. W. Chang, X. Yu, P. Wu, R. X. Shen, L. Z. Wang, X. Z. Cui and J. L. Shi, *Adv. Sci.*, 2025, **12**, 202416386.

17 X. Y. Zhao, Q. Geng, F. Dong, K. Zhao, S. Chen, H. T. Yu and X. Quan, *Chem. Eng. J.*, 2023, **466**, 143314.

18 H. B. Zhu, J. J. Wang, Z. Xu, Y. W. Tan and J. C. Wang, *Small*, 2024, **20**, 2404919.

19 Y. Lee, J. Theerthagiri, N. Yodsin, A. Min, C. J. Moon, S. Jungsuttiwong and M. Y. Choi, *Angew. Chem. Int. Ed.*, 2024, **63**, e202413774.

20 J. J. Wang, K. Liao, Y. N. Wei, G. S. Wang, Z. Y. Wan, B. Liu, Z. H. Liu, X. F.

Deng, X. Zhao and H. B. Zhang, *Adv. Funct. Mater.*, 2025, DOI: 10.1002/adfm.202516068, e16068.

21 J. Kim, J. Cherusseri, J. Theerthagiri, A. Kumar and M. Y. Choi, *Chem. Eng. J.*, 2025, **525**, 170119.

22 H. J. Zhang, J. Ran, Y. X. Ding, L. Zhou, H. Y. Wang, Y. H. Wang, Y. Y. Cao and Y. Wang, *Appl. Catal. B: Environ. Energy*, 2026, **381**, 125830.

23 J. Q. Zhao, D. X. Cao, J. X. Yao, K. Zhu and H. Zhao, *Chem. Eng. J.*, 2025, **503**, 158692.

24 R. Zhang, Y. Guo, S. C. Zhang, D. Chen, Y. W. Zhao, Z. D. Huang, L. T. Ma, P. Li, Q. Yang, G. J. Liang and C. Y. Zhi, *Adv. Energy Mater.*, 2022, **12**, 2103872.

25 X. Y. Fan, C. Z. Liu, Z. X. Li, Z. W. Cai, L. Ouyang, Z. R. Li, X. He, Y. S. Luo, D. D. Zheng, S. J. Sun, Y. Wang, B. W. Ying, Q. Liu, A. Farouk, M. S. Hamdy, F. Gong, X. P. Sun and Y. Y. Zheng, *Small*, 2023, **19**, 2303424.

26 J. L. Wei, Y. J. Liu, Z. Wu, L. H. Han, A. M. Deng, Q. Y. Li, C. M. Jiang, J. J. Liu, L. Gan, Y. Q. Zhang and S. Y. Wang, *Adv. Funct. Mater.*, 2025, DOI: 10.1002/adfm.202513566, e13566.

27 H. X. Lin, J. S. Wei, Y. Guo, Y. Li, X. H. Lu, C. C. Zhou, S. Q. Liu and Y. Y. Li, *Adv. Funct. Mater.*, 2024, **34**, 2409696.

28 K. Huang, K. Tang, M. H. Wang, Y. J. Wang, T. T. Jiang and M. Z. Wu, *Adv. Funct. Mater.*, 2024, **34**, 2315324.

29 J. N. Lv, Q. W. Yang, T. T. Liang, X. T. Sun, W. T. Rong, Q. Q. Dai, Y. Z. Gao, L. F. Wang, X. H. Xu and Y. Liu, *J. Am. Chem. Soc.*, 2025, **147**, 27708-27719.